Lattice investigation of the Das-Mathur-Okubo sum rule

Walter Wilcox
Department of Physics, Baylor University, Waco, Texas 76798-7316
(Received 24 November 1997; published 4 May 1998)

An evaluation of charged pion polarizability using correlation functions measured on a $16^3\times 24$ lattice in the context of the Das-Mathur-Okubo sum rule is carried out. The calculation is limited to the so-called intrinsic part of the polarizability. This contribution, equivalent to a Euclidean time integral over vector and axial vector momentum-differentiated propagators, is evaluated in both a continuous and discrete sense. In the continuous case, the time behavior of the correlation functions is fit to the continuum quark model; the discrete case is handled by a straightforward application of Simpson's rule for integration after subtracting the pion contributions. A comparison of the implied vector meson and pion decay constants with phenomenological values is carried out. Results for the intrinsic polarizability are extrapolated across four quark mass values to the chiral limit. An extensive discussion of the lattice systematics in this calculation is given. [S0556-2821(98)03611-X]

PACS number(s): 12.38.Gc, 11.15.Ha, 11.55.Hx

I. INTRODUCTION

Charged pion polarizability is a fascinating laboratory for strong interaction physics. It sits at the crossroads of experiment, dispersion relations, sum rules and chiral model results. It also can be evaluated on the lattice and turns out to be a sensitive barometer of such inputs as lattice scale, ground state mass values, and models for fitting propagator data. It is therefore both an excellent testbed for investigating gauge lattice systematics as well as an extremely interesting and fundamental dynamical quantity in itself.

Some previous experimental and theoretical results on charged pion polarizability ($\alpha_{\pi^\pm}$) are presented in Table I. Both experimental and theoretical disagreements are evident. It is thus an opportune time to initiate lattice studies which attempt to calculate this quantity from first principles [9,10]. Excellent reviews of the experimental and theoretical situations are available [11].

External field methods have been used previously to measure neutral particle polarizabilities in the context of lattice QCD [12]. Of course these methods would be very difficult or impossible to use in the case of charged hadrons because charged particles accelerate in an electric field. The evaluation of charged particle polarizabilities can be done directly on the lattice by measuring a Compton scattering coefficient [10]. However, the direct evaluation is actually quite involved because of the many disconnected diagrams involved. There is a way around this difficulty if one is willing to work in the exact chiral limit by use of the Das-Mathur-Okubo (DMO) sum rule [13]. Although this results in a simpler lattice calculation, a well-known problem in this approach is that the spectral integral involves a rather precise cancellation of large numbers and so may be difficult to evaluate numerically. This paper attempts to understand to what extent this difficulty holds in lattice evaluations and to begin to explore the internal systematics of such calculations.

An explanation of the methods used to estimate the DMO spectral integral will be given in the next section. Successful use of the quark continuum model will be made; this sheds additional light on its use and range of validity. The consistency of the results will be probed using an alternate purely numerical approach based on Simpson's rule. We will also check the consistency of our data with low energy phenomenology by extracting the pion and rho meson decay constants, f_π and f_ρ, from the axial and vector correlation functions. Various other sources of systematic error will be estimated and suggestions for further improvements in future lattice evaluations of charged pion polarizability will be made.

II. BACKGROUND

A. Review

The DMO sum rule for the charged pion polarizability, derived from current algebra in the chiral limit, is

$$\alpha_{\pi^\pm}=\alpha\frac{\langle r_\pi^2\rangle}{3m_\pi}-\frac{\alpha}{2m_\pi f_\pi^2}\int_{(m_\pi+\epsilon)^2}^{\infty}\frac{ds^2}{s^4}[\rho_V(s^2)-\rho_A(s^2)]. \tag{1}$$

The pion pole is absent from the axial vector spectral integral; this is symbolized by the lower limit, $(m_\pi+\epsilon)^2$, ϵ being a small positive quantity. A conventional lattice normalization for the spectral functions $\rho_{V,A}$ is being used here; see Eq. (3) below.

There are several advantages to using Eq. (1) instead of attempting direct evaluations of pion polarizability. Equation (1) employs only mesonic two-point functions, which are

TABLE I. Previous experimental and theoretical results on charged pion polarizability.

$\alpha_{\pi^\pm}$ (10^{-4} fm^3)	Type	Reference
$6.8\pm 1.4\pm 1.2$	Expt.	Ref. [1]
$20\pm 12\pm 1.2$	Expt.	Ref. [2]
$2.2\pm 1.6\pm 1.2$	Expt.	Ref. [3, 4]
$2.64\pm .36$	Theor./Expt.	Ref. [5]
~ 3.6	Theor.	Ref. [6]
2.4 ± 0.5	Theor.	Ref. [7]
5.6 ± 0.5	Theor.	Ref. [8]

easily calculable on the lattice. In addition, the necessary propagators can be precisely measured using a combination of numerical techniques which will be explained in Sec. III A.

There is no unique way of evaluating Eq. (1) on the lattice. The strong interaction parameters, pion mass (m_π), pion decay constant (f_π) and the charged pion squared charge radius ($\langle r_\pi^2 \rangle$) also enter this expression. All these quantities can and should have separate lattice evaluations. In the limited point of view adopted here, evaluation of the spectral integral in Eq. (1), the so-called intrinsic part,

$$\alpha_{\pi^\pm}^{int} \equiv -\frac{\alpha}{2m_\pi f_\pi^2} \int_{(m_\pi+\epsilon)^2}^{\infty} \frac{ds^2}{s^4}[\rho_V(s^2)-\rho_A(s^2)], \quad (2)$$

will be concentrated on. We will also compare the implied values for the pion decay constant f_π and vector meson decay constant f_ρ against experimental results. Normally since polarizability scales like a^3, one expects it to be very sensitive to the lattice scale. However, because experimental values of m_π and f_π will be used in the DMO expression for $\alpha_{\pi^\pm}^{int}$ there will actually be no scale uncertainty in the answer obtained here. The only quantity for which we will need the lattice scale will be in the later lattice calculation of f_π.

B. Derivation

The Minkowski space DMO sum rule spectral densities $\rho_V(s^2)$ and $\rho_A(s^2)$ arise from [14]

$$\begin{aligned} i\int d^4x e^{-i\vec{k}\cdot\vec{x}}(0|T[v_\mu^3(x)v_\nu^{3\dagger}(0)-a_\mu^3(x)a_\nu^{3\dagger}(0)]|0) \\ = \frac{1}{2}\int_{(m_\pi+\epsilon)^2}^{\infty} \frac{ds^2}{\vec{k}^2+s^2}[\rho_V(s^2)-\rho_A(s^2)] \\ \times\left(-g_{\mu\nu}+\frac{k_\mu k_\nu}{s^2}\right)-\frac{f_\pi^2 k_\mu k_\nu}{\vec{k}^2+\mu^2}, \end{aligned} \quad (3)$$

where $k_0 \equiv \sqrt{s^2+\vec{k}^2}$ or $k_0 \equiv \sqrt{\mu^2+\vec{k}^2}$ (μ = pion mass) in the pion term. Also in Eq. (3) the metric is $g_{\mu\nu}=(+,-,-,-)$, $v_\mu^a(x)=\overline{\psi}(x)\frac{\tau^a}{2}\gamma_\mu\psi(x)$, and $a_\mu^a(x)=\overline{\psi}(x)\frac{\tau^a}{2}\gamma_5\gamma_\mu\psi(x)$. The $\mu,\nu=0$ amplitude can also be expressed as

$$\begin{aligned} i\int d^4x e^{-i\vec{k}\cdot\vec{x}}(0|T[v_0^3(x)v_0^{3\dagger}(0)-a_0^3(x)a_0^{3\dagger}(0)]|0) \\ = \frac{i}{2}\int d^4x(0|T[v_0^{ud}(x)v_0^{ud\dagger}(0)-a_0^{ud}(x)a_0^{ud\dagger}(0)]|0) \end{aligned} \quad (4)$$

in the exact $SU(2)$-flavor limit because of either canceling or vanishing self-contractions of the currents. The currents being used in Eq. (4) are $v_0^{ud}(\vec{x},t)\equiv\overline{d}(\vec{x},t)\gamma_0 u(\vec{x},t)$ and $a_0^{ud}(\vec{x},t)\equiv\overline{d}(\vec{x},t)\gamma_5\gamma_0 u(\vec{x},t)$. It is noticed that [15]

$$\begin{aligned} \int_{(m_\pi+\epsilon)^2}^{\infty} \frac{ds^2}{s^4}[\rho_V(s^2)-\rho_A(s^2)] \\ = i\frac{d}{d\vec{k}^2}\int_{-\infty}^{\infty} dt[\Delta_{00}^V(\vec{k}^2,t)-\Delta_{00}^A(\vec{k}^2,t)]|_{\vec{k}^2=0}, \end{aligned} \quad (5)$$

where

$$\Delta_{00}^V(\vec{k}^2,t) \equiv \int d^3x e^{-i\vec{k}\cdot\vec{x}}(0|T[v_0^{ud}(x,t)v_0^{ud\dagger}(0)]|0), \quad (6)$$

$$\Delta_{00}^A(\vec{k}^2,t) \equiv \int d^3x e^{-i\vec{k}\cdot\vec{x}}(0|T[a_0^{ud}(x,t)a_0^{ud\dagger}(0)]|0). \quad (7)$$

Last of all, a switch is made to imaginary time,

$$i\int_{-\infty}^{\infty} dt\Delta_{00}(\vec{k}^2,t) = \int_{-\infty}^{\infty} dt_E \Delta_{44}(\vec{k}^2,t_E), \quad (8)$$

where we have the standard ud-flavor propagators (real and positive for $t_E \neq 0$)

$$\Delta_{44}^V(\vec{k}^2,t_E) \equiv \int d^3x e^{-i\vec{k}\cdot\vec{x}}(0|T[v_4^{ud}(x,-it_E)v_4^{ud\dagger}(0)]|0), \quad (9)$$

$$\Delta_{44}^A(\vec{k}^2,t_E) \equiv \int d^3x e^{-i\vec{k}\cdot\vec{x}}(0|T[a_4^{ud}(x,-it_E)a_4^{ud\dagger}(0)]|0). \quad (10)$$

(One may take $\gamma_0=\gamma_4$ here.) Thus, putting Eqs. (2)–(10) together, we have

$$\begin{aligned} \alpha_{\pi^\pm}^{int} = -\frac{\alpha}{2m_\pi f_\pi^2}\frac{d}{d\vec{k}^2} \\ \times\int_{-\infty}^{\infty} dt_E[\Delta_{44}^V(\vec{k}^2,t_E)-\Delta_{44}^A(\vec{k}^2,t_E)]|_{\vec{k}^2=0}. \end{aligned} \quad (11)$$

On the lattice, the right-hand side of Eq. (11) will be formed by taking a numerical momentum derivative of the lattice propagator data. Although the derivative in Eq. (5) removes the pion contribution in Eq. (3), one has only finite momenta on the lattice and the pion contribution must be explicitly subtracted from the axial vector propagators in the lattice version of Eq. (11).

C. Continuum model

The time integral in Eq. (11) will be performed in both a discrete and continuous sense using the lattice data; the difference will be taken as a reasonable estimate of the systematic error of the integral. In the discrete case, one can simply apply Simpson's integration rule to the Euclidean time propagator data after subtracting out the pion contributions. This will be described in detail later. The continuous case demands some way of interpolating between the propagator time values. For this purpose, let us consider the standard

lattice Euclidean ud-flavor point-to-point charge density correlator ($\vec{q}=\vec{k}a$):

$$\sum_{\vec{x}} e^{-i\vec{q}\cdot\vec{x}}\langle 0|T[v_4^{ud}(x)v_4^{ud\dagger}(0)]|0\rangle.$$

One may show that this reduces to (replacing the sum $\Sigma_{\vec{x}}$ by the integral $\int d^3x$)

$$\int d^3x e^{-i\vec{q}\cdot\vec{x}} Tr[S(x,0)\gamma_4\gamma_5 S^\dagger(x,0)\gamma_4\gamma_5],$$

where $S(x,y)$ is the quark propagator and the trace is over color and Dirac spaces. Using the free quark propagator (coordinate gauge, diagonal to this order in color space),

$$S(x,0)=\frac{1}{2\pi^2}\frac{\gamma\cdot x}{x^4}+\frac{1}{(2\pi)^2}\frac{m_q}{x^2}+\cdots, \tag{12}$$

the following definition ($q\equiv|\vec{q}|$) is now made:

$$G_{44}(t,q)\equiv\int d^3x e^{-i\vec{q}\cdot\vec{x}}\frac{t^2-r^2}{(r^2+t^2)^4}. \tag{13}$$

Doing the angular integrations yields

$$G_{44}(t,q)=\frac{12}{\pi^3 q}\int_0^\infty dr\, r\,\sin(qr)\left\{\frac{2t^2}{(r^2+t^2)^4}-\frac{1}{(r^2+t^2)^3}\right\}. \tag{14}$$

Actually, what one wants in this case is a derivative of the above with respect to squared spatial momentum [see Eq. (11) above] evaluated at zero momentum. Since only finite momenta are available in the lattice simulation, this continuum procedure cannot be reproduced on the lattice. Thus in order to compare with the lattice data consider, instead,

$$\Delta G_{44}(t,q)\equiv\frac{G_{44}(t,q)-G_{44}(t,0)}{q^2}, \tag{15}$$

where q represents the lowest lattice momentum value. Fitting the lattice data with Eq. (15) has the advantage of using the same type of ''derivative'' as in the lattice data, but has the disadvantage of including a small momentum dependence in the phenomenological model. To this order the same functional form holds for the axial vector propagator as well. The next nonvanishing term in the lattice propagator from Eq. (12) is proportional to the square of the quark mass, but this term gives negligible contribution to the fits and is not considered further.

A number of modifications are necessary to this function before one compares to the lattice data. First, it is clear that the above expressions have an ultraviolet infinity associated with the $r=0$ lower limit for $t=0$. This infinity can be controlled, as the lattice itself controls it, by putting in a short distance cutoff. So replace the lower limit above by $r_0>0$, which becomes a parameter in the fits. Call this modified function $\Delta G_{44}(t,q,r_0)$. Second, put in a continuum threshold, s_0, to control the onset of excited states in the spectral density. One can show that the resulting function is given by

$$\Delta\mathcal{G}_{44}(t,q,r_0,s_0)=\int_{s_0}^\infty ds\int_{-\infty}^\infty\frac{du}{2\pi}e^{ius}\Delta G_{44}(|t|+iu,q,r_0). \tag{16}$$

A third parameter, ξ, will be introduced as a multiplicative factor normalizing this function. Originally, this parameter was introduced to account for lattice anisotrophy at small lattice time separations (see Ref. [16]). However, for an interesting alternate interpretation of this parameter, see Ref. [17]. One can analytically perform the two integrations in Eq. (16); the remaining oscillating radial integration is done numerically. This numerical evaluation makes the fitting of parameters for this model rather slow and renders a third-order jackknife analysis of the data impractical. For a more explicit representation of the function defined in Eq. (16), see the Appendix.

In attempting to fit the (momentum differentiated) propagator time data, pole mass terms of the form

$$(\lambda_\rho^q)^2e^{-E_\rho t}+(\lambda_V^q)^2e^{-E_V t} \tag{17}$$

will be added in the vector case and the three terms

$$(\lambda_\pi^q)^2e^{-E_\pi t}-(\lambda_\pi^0)^2e^{-m_\pi t}+(\lambda_A^q)^2e^{-E_A t} \tag{18}$$

will be added in the axial case. The E_ρ term [in Eq. (17)] and the E_π, m_π terms [in (18)] represent the lowest pole contributions to the spectral integral in the vector and axial vector channels. (There is no term proportional to $e^{-m_\rho t}$ in the vector case because of charge conservation.) The additional pole terms in these expressions, the E_V term in Eq. (17) and the E_A term in Eq. (18), were found to be necessary in achieving a reasonable fit to the lattice data; see the comments in Sec. III B. The mass values m_π and m_ρ will be fixed from independent lattice measurements, and the continuum relationship

$$E_\pi a=\sqrt{\vec{q}^2+(m_\pi a)^2} \tag{19}$$

will be assumed. Phenomenologically, the E_V pole in the vector case has quantum numbers of radially excited states of the rho meson and the E_A pole has the quantum numbers of the a_1 meson. All told, there are 6 parameters in the vector fits $(\xi_V,s_{0,V},r_{0,V},\lambda_\rho^q,\lambda_V^q,E_V)$ and 7 parameters $(\xi_A,s_{0,A},r_{0,A},\lambda_\pi^0,\lambda_\pi^q,\lambda_A^q,E_A)$ in the axial fits. (However, see later comments about the continuum relation between λ_π^0 and λ_π^q in Sec. III C.) Of course, once the axial data are fit, one must eliminate the pole terms involving the pion before doing the DMO integral.

In the context of the continuum plus pole model, the Euclidean lattice data are now fit to the forms

$$\Delta_{44}^V(\vec{q}^2,t)-\Delta_{44}^V(0,t)\equiv q^2\xi_V\Delta\mathcal{G}_{44}(t,q,r_0,s_0)+(\lambda_\rho^q)^2e^{-E_\rho t}+(\lambda_V^q)^2e^{-E_V t}, \tag{20}$$

$$\Delta_{44}^A(\vec{q}^2,t)-\Delta_{44}^A(0,t)\equiv q^2\xi_A\Delta\mathcal{G}_{44}(t,q,r_0,s_0)+(\lambda_\pi^q)^2e^{-E_\pi t}-(\lambda_\pi^0)^2e^{-m_\pi t}+(\lambda_A^q)^2e^{-E_A t}. \tag{21}$$

Let $\overline{\Delta_{44}^V}(\vec{q}^2,t)$ and $\overline{\Delta_{44}^A}(\vec{q}^2,t)$ represent the actual correlation functions measured on the lattice. It is assumed that these are

related to the continuum functions needed in Eq. (11) by scale, tadpole and renormalization factors as follows:

$$a^3\Delta_{44}^V(\vec{k}^2,t)=\frac{N_T}{N_s}\left[\frac{(1-0.82\alpha_V)}{4}\right]^2\overline{\Delta}_{44}^V(\vec{q}^2,t), \tag{22}$$

$$a^3\Delta_{44}^A(\vec{k}^2,t)=\frac{N_T}{N_s}\left[\frac{(1-0.31\alpha_V)}{4}\right]^2\overline{\Delta}_{44}^V(\vec{q}^2,t), \tag{23}$$

where α_V is the strong interaction coupling constant defined in Ref. [18], N_s is the number of spatial sites smeared over in the source interpolation fields (16^2 in this case), and

$$N_T=16\left(1-\frac{3\kappa}{4\kappa_{cr}}\right)^2. \tag{24}$$

We will use $\alpha_V(\pi/a)=0.1557$ ($\beta=6.0$) for the local currents in this study. In the following tables and figures, the results for the intrinsic part of the charged pion polarizability will presented in natural dimensionless form, $\mathcal{I}_{V,A}$, where

$$\alpha_{\pi^\pm}^{intr}=\frac{\alpha}{m_\pi f_\pi^2}(\mathcal{I}_A-\mathcal{I}_V), \tag{25}$$

$$\mathcal{I}_{V,A}\equiv\frac{1}{2}\int_{(m_{\pi^+}+\epsilon)^2}^{\infty}\frac{ds^2}{s^4}\rho_{V,A}(s^2). \tag{26}$$

III. RESULTS

A. Simulation parameters

The simulation was done on 32 quenched configurations with Wilson fermions on a $16^3\times 24$ lattice at $\beta=6.0$. The lattices were constructed with the algorithm of Ref. [19], thermalized by 11 000 sweeps and separated by 1000 sweeps. Four values of the Wilson hopping parameter were considered, $\kappa=0.154$, 0.152, 0.150 and 0.148. We used the ''volume method'' [20,21] to calculate the propagators directly from the nongaugefixed configurations, smearing over a 16×16 spatial plane at time step 8 of the lattice. (The first time step of the lattice will be defined to be $t\equiv 1$.) This sacrifices the Fourier transforms in two spatial directions but reinforces the momentum projection in the third. This is the main idea of the ''Fourier reinforcement'' method [22].

The signals obtained for the vector and axial vector charge density operators are excellent. Figures 1 and 2 show the local lattice energy,

$$E^{latt}\left(t+\frac{1}{2}\right)\equiv\ln\left(\frac{\overline{\Delta}_{44}(\vec{q}^2,t)}{\overline{\Delta}_{44}(\vec{q}^2,t+1)}\right), \tag{27}$$

for the vector and axial vector cases, respectively. The ρ and π masses were calculated separately with extremely long time base lines on 20 of these configurations, fixed to the lattice Coulomb gauge, with quark propagators starting at $t=1$ and single exponential fits to time steps 16–19. The results are given as the first line in Tables II and III. Three of these results ($\kappa=0.154$, 0.152, 0.148) are taken from Table I of Ref. [23]; the result at $\kappa=0.150$ is new. The value of $\kappa_{cr}=0.1564$ is also taken from Ref. [23]. The dimensionless quark mass in this reference as well as here is taken to be

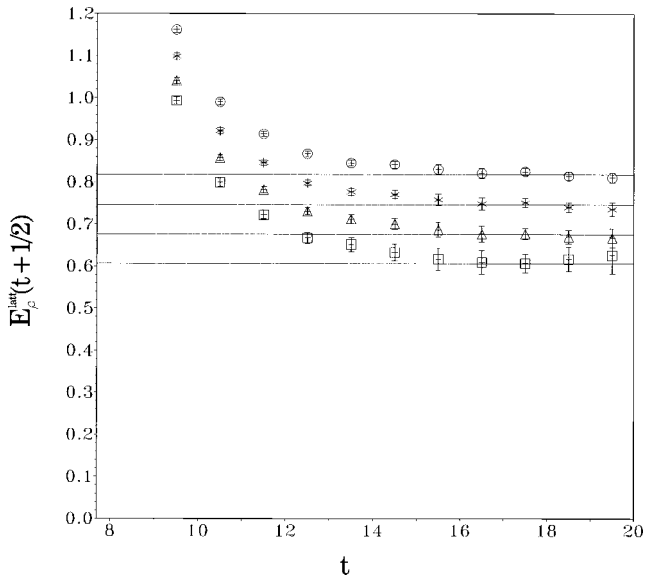

FIG. 1. Local $E_\rho^{latt}(t+\frac{1}{2})$ measurements for the lattice vector charge density, $\overline{\Delta}^V(\vec{q}^2,t)$, versus lattice time location, t, compared with continuum dispersion (horizontal lines) for $|\vec{q}|=\pi/8$. Squares are for $\kappa=0.154$, triangles are $\kappa=0.150$, stars are for $\kappa=0.148$, and circles are $\kappa=0.148$ results.

$$ma\equiv\ln\left(\frac{4\kappa_{cr}}{3\kappa}-3\right). \tag{28}$$

The correlated chi-squared per degree of freedom, χ_d^2, on all of the mass fits [no singular value decomposition (SVD) decomposition; see Sec. III B], were less than one. The horizontal lines in Figs. 1 and 2 show the predicted energies using continuum dispersion; agreement with the lattice data on time steps 15–20 inclusive is evident. These masses will be used as fixed input rather than parameters in the present calculation, which significantly improves the error bars on

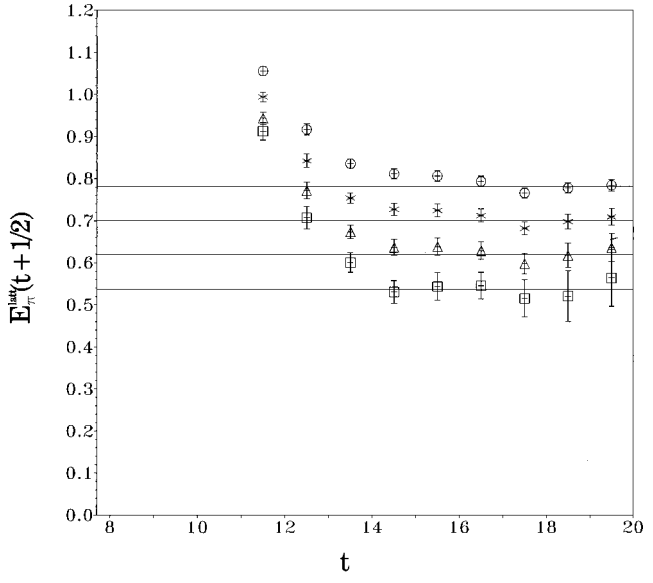

FIG. 2. Local $E_\pi^{latt}(t+\frac{1}{2})$ measurements for the lattice axial vector charge density, $\overline{\Delta}^A(\vec{q}^2,t)$, versus lattice time location, t, compared with continuum dispersion (horizontal lines) when $|\vec{q}|=\pi/8$. Symbols are the same as in Fig. 1.

TABLE II. Continuum model vector fit parameters. χ_d^2 gives the chi-squared per degree of freedom for the fit.

Quantity	$\kappa=0.154$	0.152	0.150	0.148
$m_\rho^{\text{input}}a$	0.463(.020)	0.550(.013)	0.635(.010)	0.718(.008)
ξ_V	4.44(.54)	4.16(.78)	3.71(.52)	3.57(.50)
$s_{0,V}$	0.90(.55)	0.568(.050)	0.644(.050)	0.724(.049)
$r_{0,V}$	0.442(.028)	0.417(.040)	0.383(.029)	0.368(.029)
λ_ρ^q	$4.86(.43)\times10^{-2}$	$4.36(.41)\times10^{-2}$	$4.65(.28)\times10^{-2}$	$4.79(.18)\times10^{-2}$
λ_V^q	$4.6(1.7)\times10^{-2}$	$4.6(1.1)\times10^{-2}$	$5.03(.62)\times10^{-2}$	$5.12(.60)\times10^{-2}$
$E_V a$	1.17(.14)	1.33(.18)	1.46(.10)	1.55(.07)
χ_d^2	0.34	0.30	0.44	0.60

the remaining fit parameters. The systematic effects of varying the input ρ and π masses in this calculation will be reported on in Sec. III C.

B. Spectral integral evaluation

The data in the vector and axial vector sectors were fit to Eqs. (20) and (21); examples of these fits are shown in Figs. 3 and 4, which show the case $\kappa=0.154$. It is the area under these curves which is of interest here. The time integrals are very sharply peaked and the fits themselves extend from the source time site at $t=8$ to $t=20$. The numerical quality of the vector time data is seen to be better than the axial vector case, but both are quite acceptable. The parameters of these fits are given in Tables II and III.

A second-order single elimination jackknife was used for error analysis at each κ value; the first order defines error bars on the time correlation functions and the second defines errors on the fit parameters of these functions. The fits reported in Tables II and III are characterized by their correlated chi-squared per degree of freedom, χ_d^2. These were arrived at by the SVD algorithm suggested in Ref. [24]. It was found there that the correct correlated χ_d^2 was obtained on small data samples when the number of exact eigenvalues retained, E, was chosen to be $\approx\sqrt{N}$, where N is the number of configurations. We will use $E=6$ ($N=32$). Defining D to be the number of fit time sites ($D=13$), Ref. [25] finds that the increase in χ_d^2 from the ''true'' result is given by $1+(D+1)/N$, which in the present case is approximately 1.44. (Comparing SVD and non-SVD fits, this ratio was actually found to be 1.57 in the vector case and 1.45 in the axial case, averaged over κ.) The χ_d^2 values in the vector case ($\sim.3-.6$) are quite good; the χ_d^2 values in the axial case ($\sim1.0-1.5$) were higher, but are still acceptable. The pole terms involving λ_V, λ_A in Eqs. (20) and (21) were crucial to obtaining acceptable fits in both the vector and axial vector sectors. The fitting of 13 time sites with acceptable χ_d^2 values including the time origin is an extremely nontrivial matter and shows the usefulness of the (cutoff) continuum quark model in fitting lattice propagator data.

As is suggested by the numerical results of Ref. [24], the best values of the fit parameters (and their error bars from the jackknife) are actually determined by doing uncorrelated fits; the correlated χ_d^2 was used only as a selection criterion of fit time intervals. This is the same procedure as used in Ref. [23]. The error bars in the parameters of the time fits were determined by the jackknife, while the errors in the fits across κ values were determined by the Levenberg-Marquardt method [26] using the CURFIT routine of Ref. [27].

Tables IV and V give the relative contribution of the various continuum model sectors to the final result. One sees that the (subtracted) axial sector is almost saturated by the assumed pole, but that only about 30% of the vector result is given by the ρ-meson pole, the majority coming from the continuum. This is very different from chiral model expectations and has important consequences for the final answer.

The fit parameter values in Tables II and III are fairly reasonable. The continuum threshold values $s_{0,V}$, $s_{0,A}$ are of order unity, with $s_{0,V}$ tending to cluster just above the ρ-meson mass; there is no particular trend in the axial case.

TABLE III. Continuum model axial fit parameters. χ_d^2 gives the chi-squared per degree of freedom for the fit.

Quantity	$\kappa=0.154$	0.152	0.150	0.148
$m_\pi^{\text{input}}a$	0.366(.010)	0.479(.008)	0.581(.007)	0.676(.0062)
ξ_A	1.5(1.7)	1.1(1.2)	0.96(.45)	0.61(1.0)
$s_{0,A}$	1.19(.24)	1.31(.18)	1.34(.17)	0.69(.23)
$r_{0,A}$	0.50(.30)	0.49(.24)	0.546(.082)	0.60(.54)
λ_π^0	$3.73(.26)\times10^{-2}$	$4.96(.25)\times10^{-2}$	$6.18(.26)\times10^{-2}$	$7.37(.25)\times10^{-2}$
λ_π^q	$5.05(.37)\times10^{-2}$	$6.10(.34)\times10^{-2}$	$7.16(.34)\times10^{-2}$	$8.15(.41)\times10^{-2}$
λ_A^q	$7.6(1.3)\times10^{-2}$	$7.95(.84)\times10^{-2}$	$8.04(.38)\times10^{-2}$	$8.22(.85)\times10^{-2}$
$E_A a$	1.38(.15)	1.49(.11)	1.58(.06)	1.70(.07)
χ_d^2	1.00	1.53	1.45	1.19

(Large fluctuations in $s_{0,V}$ occur at $\kappa=0.154$ in the vector case although the jackknife error in the final integral remains quite small; see Table VII.) The E_V, E_A pole energies, mimicking the contribution of higher bound states, are seen to decrease with increasing κ. The values of λ_ρ^q, λ_π^0 and λ_π^q are also reasonable and will be examined extensively in Sec. III C. However, there are also some questionable aspects to the parameter values in Tables II and III. In the interpretation of Ref. [16], the $\xi_{V,A}$ values should be approximately constant across κ. In fact, there is an increase in these values as κ increases in these tables, although the axial case is dominated by errors. (Note that the $\xi_{V,A}$ values are significantly decreased by the inclusion of the $\lambda_{V,A}^q$ pole terms.) In addition, the short distance cutoff values $r_{0,V}$ and $r_{0,A}$ are not particularly constant in κ as one might expect. The axial case $r_{0,A}$ values are dominated by errors and no real comparison between the two sets of values can be made.

As a completely independent means of approaching these integrals, the Simpson integration formula for discrete data [26] was utilized. In order to do this, it is necessary to explicitly remove the pion poles in the zero momentum and nonzero momentum axial vector propagators. These were fit with single exponentials (using the SVD decomposition) to the 18–20 time sites, with acceptable correlated χ_d^2 values in both cases. Table VI reports the results of these evaluations. The λ_π^0, λ_π^q values reported in this table are then used to remove the pion tails from the axial vector propagator time integrals. There is no unique way of numerically integrating the subtracted data. Since the lattice data are so strongly peaked in time, different integration rules can give significantly different results. The Simpson rule was chosen because it was simple and well known, but other rules could have served as well. The choice of an odd number of time sites to fit (13) means that the discontinuities in the fit polynomials will occur at odd time sites, including the origin. This allows for the strong peaking near the time origin seen in Figs. 3 and 4 and gives much better agreement with the continuum model integral results than an integral rule which requires continuity at the origin.

Figure 5 shows the final chiral extrapolations in κ, with numerical results reported in Table VII. This table shows that the Simpson and continuum results for $\mathcal{I}_V$ are rather close, whereas $\mathcal{I}_A$ is the major source of the systematic error in the time integral. The statistical errors in $\mathcal{I}_A$ are also significantly larger than those in $\mathcal{I}_V$. The continuum model values are shown as squares, the Simpson evaluations as circles, with the solid symbols representing the extrapolated values. The Simpson values are larger but extrapolate to a smaller result because of the positive slope. On the other hand the continuum model results have a more sedate, negative slope. Combining these results, the dimensionless integral $\mathcal{I}\equiv\mathcal{I}_V-\mathcal{I}_A$ is now given as

$$\mathcal{I}=36.3(3.9)(3.5)\times10^{-3}, \tag{29}$$

implying (using $m_\pi=139.6$ MeV, $f_\pi=92.4$ MeV)

$$\alpha_{\pi^\pm}^{int}=-17.1(1.8)(1.6)\times10^{-4}\ \text{fm}^3, \tag{30}$$

where the first number in parentheses is the statistical error and the second is the systematic error, taken to be half of the difference of the continuum and Simpson model central values. The central value and the statistical error are the average of the continuum and Simpson results from Table VII. The central value in Eq. (29) is significantly larger than current experimental or chiral results would imply. For example, Ref. [5] quotes $27.0(.5)\times10^{-3}$ and Ref. [8] gives $21.0(.5)\times10^{-3}$ for this same quantity. When combined with the experimental result $\langle r_\pi^2\rangle=0.439(.008)$ fm^2 from Ref. [28], this implies a negative pion polarizability, $\alpha_{\pi^\pm}=-2.0(1.8)\times(1.6)\times10^{-4}$ fm^3. [The result $\langle r_\pi^2\rangle=0.463(.006)$ fm^2 from Ref. [29] would imply $\alpha_{\pi^\pm}=-1.2(1.8)(1.6)\times10^{-4}$ fm^3.] We will explore the systematics responsible for this outcome in the next subsection.

C. Systematics

The pion and rho meson masses listed as the top lines in Tables II and III are themselves measured from the lattice and have their own Monte Carlo statistical errors. Since these are treated as input rather than fit parameters, one should investigate the systematic errors associated with varying these inputs. This is done by studying the change in the central value of the chiral-extrapolated result, Eq. (29), when the rho and pion masses are put at the upper and lower limits in Table III. When this is done with the rho meson, the central value changed by approximately $\pm1\%$. As one might expect, the result of Eq. (29) is more sensitive to the input pion mass because this is used to fit and remove the pion spectral contribution. It is found that the results from the continuum quark model are considerably more sensitive to the input pion mass than the Simpson results. By varying the pion mass within the limits in Table III one finds that the central value of the result in Eq. (29) changes by (symmetrizing the upper and lower changes) by about $\pm2.3\%$. This is small compared to the estimated systematic uncertainty due to the integral model (continuum or Simpson) dependence.

In order to estimate the size of the finite lattice spacing errors in this simulation, we replaced the continuum relation (19) with the lattice spin 0 dispersion relation [30]

$$\sinh^2\left(\frac{Ea}{2}\right)=\sinh^2\left(\frac{ma}{2}\right)+\sum_i\ \sin^2\left(\frac{p_ia}{2}\right), \tag{31}$$

and made the substitution [31]

$$q\to2\sin\left(\frac{q}{2}\right), \tag{32}$$

everywhere for the momentum factor. When these changes were made, the central value in Eq. (29) was increased by approximately 2.5%.

As a consistency check of the correlation functions used in this study with low energy phenomenology, the values of the vector meson and pion decay constants have been measured and compared to experiment. The vector meson case will be especially revealing since this is a dimensionless quantity independent of the lattice scale.

The continuum matrix element for rho meson decay is given by

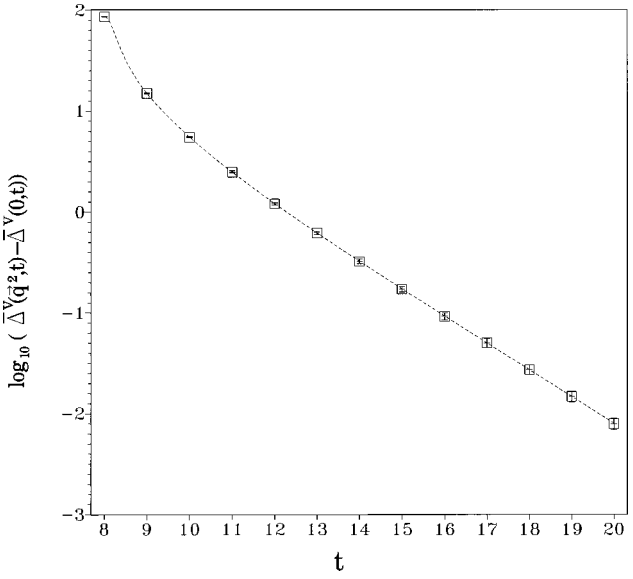

FIG. 3. The base 10 logarithm of the difference in nonzero and zero momentum lattice vector charge densities, $\log_{10}[\overline{\Delta^V}(\vec{q}^2,t) - \overline{\Delta^V}(0,t)]$, at $\kappa = 0.154$ as a function of lattice time location. The continuum model fit is shown.

$$(0|v_\mu^{ud}(0)|\rho^\lambda(\vec{p})) = \frac{m_\rho^2}{f_\rho}\frac{1}{\sqrt{2E_\rho}}\epsilon_\mu(p,\lambda), \tag{33}$$

where f_ρ is the decay constant, the polarization state is specified by λ and $\mu = 0$ for the charge density operator. One can show that in terms of the λ_ρ^q parameter in the continuum fits, the implied vector meson decay constant is given by

$$f_\rho = \frac{q(m_\rho a)}{\lambda_\rho^q \sqrt{2(E_\rho a)}} \tag{34}$$

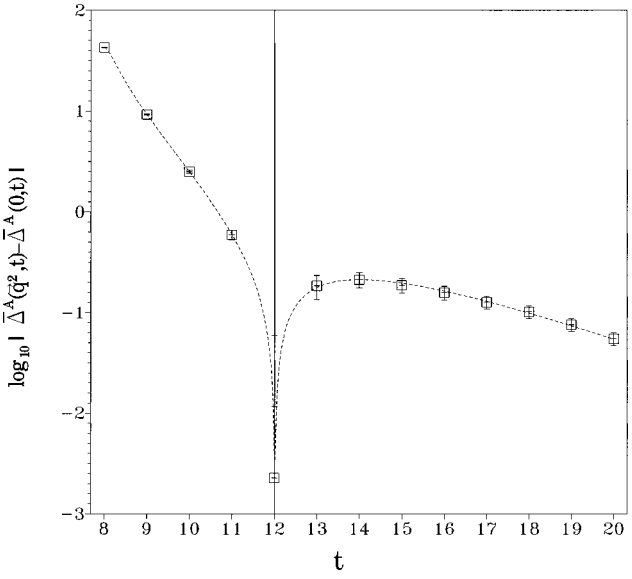

FIG. 4. The base 10 logarithm of the absolute value of the difference between nonzero and zero momentum lattice axial vector charge densities, $\log_{10}|\overline{\Delta^A}(\vec{q}^2,t) - \overline{\Delta^A}(0,t)|$, at $\kappa = 0.154$ as a function of lattice time location. The continuum model fit is shown. Notice the change in sign of the correlation function slightly after time location 12.

TABLE IV. Continuum model vector integral strengths.

Contribution	$\kappa = 0.154$	0.152	0.150	0.148
Continuum	0.51(.18)	0.61(.09)	0.56(.06)	0.55(.05)
Lowest pole	0.34(.06)	0.25(.05)	0.27(.03)	0.28(.02)
Excited pole	0.16(.13)	0.14(.05)	0.16(.03)	0.17(.04)

where $q = \pi/8$. The results for the vector meson decay constant, f_ρ, are given in Table VIII and are shown in Fig. 6. When all 4 κ values are extrapolated to κ_{cr}, we obtain $f_\rho = 3.11(.39)$ ($\chi_d^2 = .59$), lower than the experimental value of 3.56(.14). However, it is well known in lattice studies on similar sized lattices that the ρ to nucleon mass ratio, m_ρ/m_N, is underestimated when extrapolated to the chiral limit. Using the nucleon mass to set the lattice scale, if one instead extrapolates f_ρ to the ρ-meson *physical* mass, about 770 MeV (occurring at about $\kappa = 0.1545$), one obtains a much better result, $f_\rho = 3.48(.28)$. We will check that the f_π values from the axial vector propagator given by this choice of scale is consistent with experimental results.

The large time limit of the axial vector propagators imply values of the pion decay constant, f_π. One has that

$$(0|a_\mu^{ud}(0)|\pi(\vec{p})) = i\frac{p_\mu f_\pi}{\sqrt{E_\pi}}, \tag{35}$$

where again $\mu = 0$. One can relate the parameter λ_π^0 to the pion decay constant as follows:

$$f_\pi = \frac{\lambda_\pi^0}{a\sqrt{m_\pi a}}. \tag{36}$$

The results of this calculation are shown in Fig. 7 ($a^{-1} = 1.74$ GeV, Ref. [32]). The extrapolation to the chiral limit is extremely straight and one obtains 87.4(9.0) MeV, consistent with the experimental result of 92.4 MeV.

As a check on the f_π calculation, we consider the ratio of the axial pole parameters for the pion, which by the continuum relation (35) is given by

$$\lambda_\pi^q/\lambda_\pi^0 = \sqrt{E_\pi/m_\pi}. \tag{37}$$

This comparison is carried out in Table IX for the continuum and Simpson fits. There appears to be a small violation of this continuum relation at perhaps the 5–10% level in the lattice data. However, note that a systematic error in this quantity does not necessarily affect the calculation since the pion contributions are excluded from the DMO axial integral. Also note that the two data treatments (continuum and Simpson) are quite consistent with one another for this ratio.

We have seen above that f_ρ, extrapolated to the chiral limit, gives a result which is small compared to experiment

TABLE V. Continuum model axial integral strengths.

Contribution	$\kappa = 0.154$	0.152	0.150	0.148
Continuum	0.28(.25)	0.20(.17)	0.18(.08)	0.16(.25)
Pole	0.72(.25)	0.80(.17)	0.82(.08)	0.84(.25)

TABLE VI. Simpson model parameters. χ_d^2 gives the chi-squared per degree of freedom for each fit.

Quantity	$\kappa=0.154$	0.152	0.150	0.148
λ_π^0	$3.70(.24)\times10^{-2}$	$4.94(.22)\times10^{-2}$	$6.23(.23)\times10^{-2}$	$7.53(.24)\times10^{-2}$
χ_d^2	0.57	0.83	0.82	0.80
λ_π^q	$4.73(.31)\times10^{-2}$	$5.95(.27)\times10^{-2}$	$7.27(.27)\times10^{-2}$	$8.63(.28)\times10^{-2}$
χ_d^2	0.19	0.15	0.13	0.09

but that the f_π value extracted using the axial propagator and the nucleon mass scale is consistent with phenomenology. This suggests that it may be the behavior of the vector propagator in the chiral limit which is responsible for the large value of $\mathcal{I}$ in this calculation. To test this, one may instead extract the value of the vector contribution $\mathcal{I}_V$ at the physical ρ-meson mass, similar to what was done above for f_ρ; we now obtain $\mathcal{I}=33.2(4.0)(2.9)$, a better result but one which is still too large. The remaining difference is clearly due to the large ''continuum'' contribution to the vector correlator remarked on earlier; see Sec. III B and Table IV.

Finally, note that the intrinsic polarizability, through the renormalization factors in Eqs. (22) and (23), is fairly insensitive to the value of α_V used since the vector and axial vector integrals contribute with opposite signs. Roughly speaking, it is found that a x% percentage change in the value of α_V induces a change in Eq. (29) of about $-x/2\%$.

IV. CONCLUSIONS AND REMARKS

The sum rule method of extracting charged pion polarizability from lattice data has been examined. In the limited point of view adopted here, the spectral integral in the DMO sum rule has been considered separately. It has been evaluated with lattice data and the result, large compared to phenomenology and chiral models, is given by Eq. (29). Smaller systematic effects from altered input mass values, finite lattice spacing and renormalization constants were also considered.

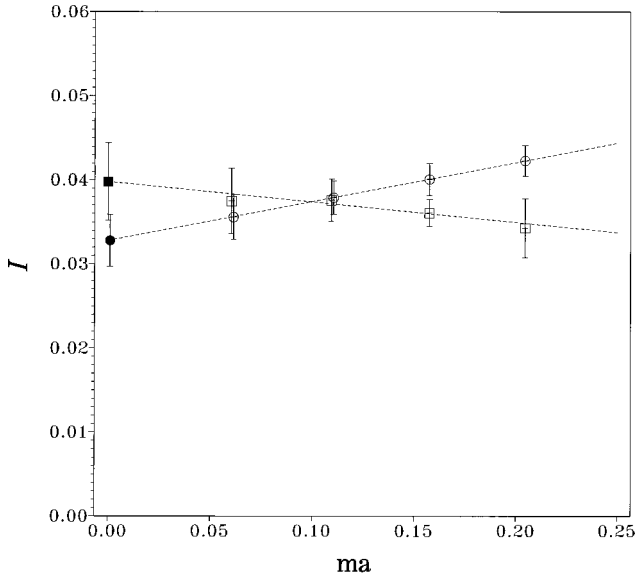

FIG. 5. Chiral extrapolation of the final results for the dimensionless spectral integral, $\mathcal{I}$, as a function of dimensionless quark mass, ma. Squares are for the continuum model results and circles are for Simpson model results from Table VII. The solid symbols represent the chiral-extrapolated results at $ma=0$. Note that some of the circles are offset in ma for clarity of presentation.

Excellent fits were obtained to the (momentum-differentiated) lattice data across 13 time slices, including the propagator origins, using the continuum quark model. The time fitting of these quantities with reasonable χ_d^2 values would not have been possible without (1) introduction of the lattice cutoff, r_0; (2) addition of additional pole terms in both the vector and axial vector cases; (3) the SVD modification, following Ref. [25], of the time propagator eigenvalues. We have also seen that the axial vector propagator is largely responsible for both the statistical and time-integral systematic errors.

The lattice systematics have been examined extensively and it has been argued above that (1) systematics associated with the incorrect lattice ratio m_ρ/m_N and (2) the fact that the vector propagator is far from being dominated by the ρ-meson are responsible for the large central value of our final result in Eq. (26). It is precisely because pion polarizability is so sensitive to and revealing of lattice systematics that it represents a significant test of the ability of the lattice to produce phenomenologically interesting predictions. Further studies with larger lattices and better actions should be even more revealing of these systematics.

It is clear that in order to obtain phenomenologically interesting values of $\alpha_{\pi^\pm}^{int}$ from the lattice, both the statistical and systematic errors here will have to be reduced. The systematic uncertainty in the time integrals can be reduced by using a time-asymmetric lattice with a fine mesh of lattice points in the time direction. This will allow sampling at smaller time intervals (but not too small to get into the asymptotic time regime) in evaluating the strongly peaked integrals. However, in order to understand the *dynamics* leading to pion polarizability, it will be necessary to go beyond the DMO sum rule to direct measurements. These ad-

TABLE VII. Results for the dimensionless integral $\mathcal{I}$; a factor of 10^{-3} multiplies all the entries. The C superscript indicates the continuum model values and the superscript S indicates values from Simpson fits.

Quantity	$\kappa_{cr}=0.1564$	$\kappa=0.154$	$\kappa=0.152$	$\kappa=0.150$	$\kappa=0.148$
$\mathcal{I}_V^C$	79.1(1.9)	74.6(1.5)	72.1(1.3)	68.5(1.3)	65.1(1.2)
$\mathcal{I}_V^S$	79.8(1.2)	76.4(.9)	74.8(.9)	72.3(.8)	69.4(.7)
$\mathcal{I}_A^C$	39.6(4.8)	37.1(4.0)	34.6(2.6)	32.4(1.5)	30.7(3.6)
$\mathcal{I}_A^S$	47.0(2.9)	40.7(2.5)	36.8(1.9)	32.1(1.8)	27.1(1.7)
$\mathcal{I}^C$	39.8(4.6)	37.5(3.9)	37.6(2.5)	36.1(1.6)	34.3(3.5)
$\mathcal{I}^S$	32.8(3.1)	35.6(2.7)	37.9(2.0)	40.1(1.9)	42.3(1.8)

TABLE VIII. Vector and pion decay constants. f_π^C indicates values inferred from continuum model fits and f_π^S values from the Simpson fits.

Quantity	$\kappa=0.154$	0.152	0.150	0.148
f_ρ	3.40(.30)	4.26(.40)	4.39(.26)	4.60(.17)
f_π^C (MeV)	107(7)	125(6)	141(6)	156(5)
f_π^S (MeV)	106(7)	124(6)	142(5)	159(5)

ditional considerations will be taken up in future publications.

ACKNOWLEDGMENTS

This work is supported in part by NSF Grant No. 9722073 and the National Center for Supercomputing Applications and utilized the SGI Power Challenge systems. The author would like to thank J. Vasut and B. Lepore for help with the continuum quark model integrals.

APPENDIX

In this brief appendix, a more explicit form of the continuum model expression for $\Delta\mathcal{G}_{44}(t,q,r_0,s_0)$ will be given.

In introducing the ultraviolet cutoff, one can make use of the procedure in Ref. [16], which gives an upper limit, Λ, in energy. The resulting expressions are rather complicated and are only defined in the limit $t\to 0$. Alternatively, one can define a short distance cutoff simply by putting a lower limit on the r-space integrals. This is the procedure followed here. Then combining Eqs. (14) and (15) of the text, we have

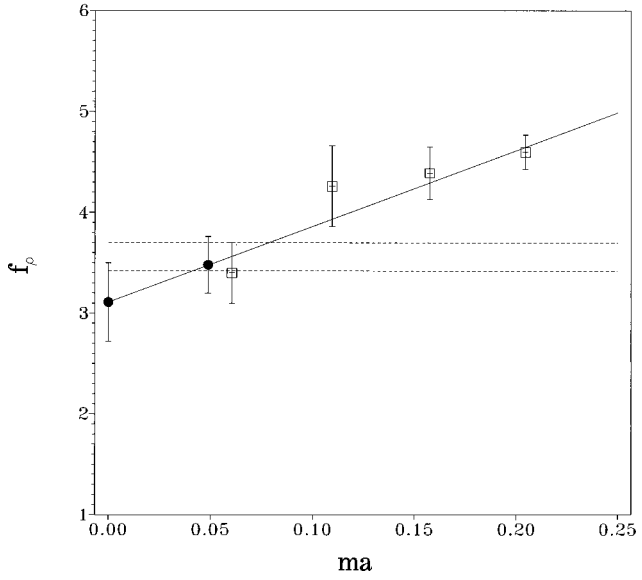

FIG. 6. The vector meson decay constant, f_ρ, as a function of dimensionless quark mass, ma. The boxes indicate measured values at $\kappa=0.154$, 0.152, 0.150 and 0.148. The solid circles indicate the extrapolated result at $ma=0$ as well as the extrapolated result at the physical ρ meson mass. The dotted line shows the experimental upper and lower limits on f_ρ.

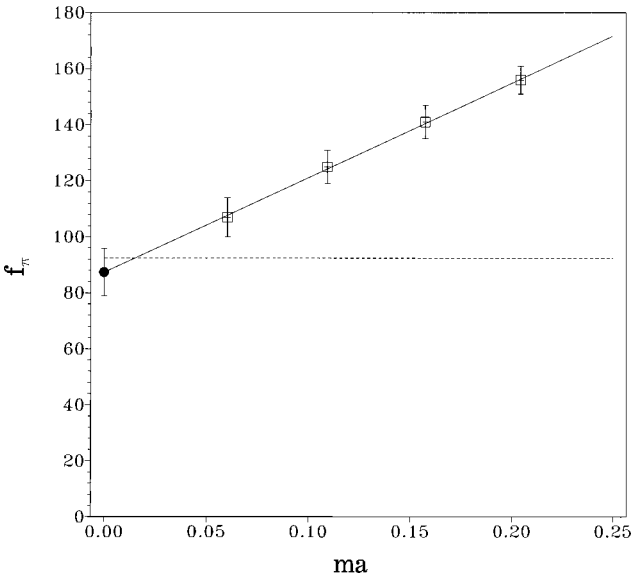

FIG. 7. The pion decay constant, f_π^C, as a function of dimensionless quark mass, ma, in MeV. The boxes indicate measured values at $\kappa=0.154$, 0.152, 0.150 and 0.148. The solid circle indicates the extrapolated result at $ma=0$ and the dotted line is the experimental result, $f_\pi=92.4$ MeV.

$$\Delta G_{44}(t,q,r_0)=\frac{12}{\pi^3 q^2}\int_{r_0}^{\infty} dr r\left(\frac{\sin(qr)}{q}-r\right)\times\left\{\frac{2t^2}{(r^2+t^2)^4}-\frac{1}{(r^2+t^2)^3}\right\}. \quad \text{(A1)}$$

The continuum threshold that is introduced in Ref. [16] is equivalent to doing an an incomplete Laplace transform of the spectral density, which is itself obtained with an inverse Laplace transform of the propagator. A similar procedure is followed here with the vector and axial vector continuum spectral densities. The basic assumption of the continuum model is that we are at low enough lattice momentum that

$$\Delta G_{44}(t,q,r_0)\xrightarrow{q^2\to 0}\int_0^\infty \frac{ds^2}{2s^3}e^{-s|t|}\rho(s^2) \quad \text{(A2)}$$

is a reasonable identification. In this limit this means that $\Delta G_{44}(t,q,r_0)$ has the time integral

$$\int_{-\infty}^{\infty} dt\,\Delta G_{44}(t,q,r_0)\xrightarrow{q^2\to 0}\int_0^\infty \frac{ds^2}{s^4}\rho(s^2), \quad \text{(A3)}$$

consistent with Eq. (3). Now putting Eq. (A1) into Eq. (16) results in the explicit expression (for $t>0$),

TABLE IX. Comparison of the continuum ratio $\lambda_\pi^q/\lambda_\pi^0$ for continuum and Simpson model axial fits.

Quantity	$\kappa=0.154$	0.152	0.150	0.148
Continuum theory	1.21	1.14	1.10	1.08
Continuum model	1.35(.10)	1.23(.06)	1.16(.05)	1.11(.04)
Simpson model	1.28(.09)	1.20(.06)	1.17(.04)	1.15(.04)

$$\Delta\mathcal{G}_{44}(t,q,r_0,s_0)=\frac{12}{\pi^3q^2}\left\{2\int_{r_0}^{\infty}drr\left(\frac{\sin(qr)}{q}-r\right)\int_{s_0}^{\infty}ds\int_{-\infty}^{\infty}du\frac{e^{ius}(t+iu)^2}{[r^2+(t+iu)^2]^3}-\int_{r_0}^{\infty}drr\left(\frac{\sin(qr)}{q}-r\right)\right.$$
$$\left.\times\int_{s_0}^{\infty}ds\int_{-\infty}^{\infty}du\frac{e^{ius}}{[r^2+(t+iu)^2]^2}\right\}. \tag{A4}$$

The poles in the u-integral are identified and the integration done. The remaining s-integral is then done explicitly. The final result can be presented as follows:

$$\Delta\mathcal{G}_{44}(t,q,r_0,s_0)=-\frac{1}{2\pi^3q^2}\mathrm{Re}\left\{\int_{r_0}^{\infty}\frac{dr}{r}\left(\frac{\sin(qr)}{q}-r\right)e^{s_0(-t+ir)}\left[\frac{6}{(t-ir)^4}+\frac{6s_0}{(t-ir)^3}+\frac{3s_0^2}{(t-ir)^2}+\frac{s_0^3}{(t-ir)}\right.\right.$$
$$\left.+\frac{3}{r^2}\left(\frac{1}{(t-ir)^2}+\frac{s_0}{(t-ir)}\right)+\frac{3i}{r^3(t-ir)}\right]\Bigg\}-\frac{3}{2\pi^3q^2}\mathrm{Im}\left\{\int_{r_0}^{\infty}\frac{dr}{r^2}\left(\frac{\sin(qr)}{q}-r\right)\right.$$
$$\left.\times e^{s_0(-t+ir)}\left[-\frac{2}{(t-ir)^3}-\frac{2s_0}{(t-ir)^2}-\frac{s_0^2}{(t-ir)}-\frac{3i}{r}\left(\frac{1}{(t-ir)^2}+\frac{s_0}{(t-ir)}\right)+\frac{3}{r^2(t-ir)}\right]\right\}. \tag{A5}$$

The explicit real and imaginary parts are then separated out from this expression and the remaining r-integration is done numerically in the continuum fits of the vector and axial vector data.

[1] Y. M. Antipov *et al.*, Phys. Lett. **121B**, 445 (1983).
[2] T. A. Aibergenov *et al.*, Czech. J. Phys. **36**, 948 (1986).
[3] J. Boyer *et al.*, Phys. Rev. D **42**, 1350 (1990).
[4] D. Babusci *et al.*, Phys. Lett. B **277**, 158 (1992).
[5] V. Kartvelishvili, M. Margvelashvili, and G. Shaw, Nucl. Phys. B (Proc. Suppl.) **54A**, 309 (1997).
[6] M. A. Ivanov and T. Mizutani, Phys. Rev. D **45**, 1580 (1992).
[7] U. Bürgi, Phys. Lett. B **377**, 147 (1996).
[8] M. J. Lavelle, N. F. Nasrallah and K. Schilcher, Phys. Lett. B **335**, 211 (1994).
[9] W. Wilcox, in *Lattice '96*, Proceedings of the International Symposium, St. Louis, Missouri, edited by C. Bernard *et al.* [Nucl. Phys. B (Proc. Suppl.) **53**, 302 (1997)].
[10] W. Wilcox, Ann. Phys. (N.Y.) **255**, 60 (1997).
[11] J. Portolés and M. R. Pennington, in ''Theoretical Predictions for Pion Polarizabilities,'' Second DAPHNE Physics Handbook, edited by L. Maiani, G. Pancheri and N. Paver (Frascati, 1995), p. 579; B. R. Holstein, Comments Nucl. Part. Phys. **19**, 221 (1990).
[12] H. R. Fiebig, W. Wilcox, and R. M. Woloshyn, Nucl. Phys. **B324**, 47 (1989).
[13] T. Das, V. S. Mathur, and S. Okubo, Phys. Rev. Lett. **19**, 859 (1967).
[14] M. V. Terent'ev, Sov. J. Nucl. Phys. **16**, 87 (1973).
[15] This corrects a minus sign error in Eq. (2) of Ref. [9].
[16] D. B. Leinweber, Phys. Rev. D **51**, 6369 (1995).
[17] C. R. Allton and S. Capitani, in Lattice '97 Proceedings of the International Symposium, Edinburgh, Scotland, edited by C. T. H. Davies *et al.* [Nucl. Phys. B (Proc. Suppl.) **63**, 263 (1998)].
[18] G. P. Lepage and P. B. Mackenzie, Phys. Rev. D **48**, 2250 (1993).
[19] N. Cabibbo and E. Marinari, Phys. Lett. **119B**, 387 (1982).
[20] Y. Kuramashi *et al.*, Phys. Rev. Lett. **71**, 2387 (1993).
[21] W. Wilcox, S. Trendafilov, and E. Mendel, in *Lattice '94*, Proceedings of the International Symposium, Bielefeld, Germany, edited by F. Karsch *et al.* [Nucl. Phys. B (Proc. Suppl.) **42**, 557 (1995)].
[22] W. Wilcox and B. Andersen-Pugh, in *Lattice '93*, Proceedings of the International Symposium, Dallas, Texas, edited by T. Draper *et al.* [Nucl. Phys. B (Proc. Suppl.) **34**, 393 (1994)].
[23] W. Andersen and W. Wilcox, Ann. Phys. (N.Y.) **255**, 34 (1997).
[24] C. Michael and A. McKerrell, Phys. Rev. D **51**, 3745 (1995).
[25] C. Michael, Phys. Rev. D **49**, 2616 (1994).
[26] W. H. Press, B. R. Flannery, S. A. Teukolsky, and W. T. Vetterling, *Numerical Recipes* (Cambridge University Press, Cambridge, England, 1986).
[27] P. R. Bevington, *Data Reduction and Error Analysis for the Physical Sciences* (McGraw-Hill, New York, 1969).
[28] S. R. Amendolia *et al.*, Phys. Lett. B **178**, 244 (1986).
[29] B. V. Geshkenbein, Z. Phys. C **45**, 351 (1989).
[30] H. J. Rothe, *Lattice Gauge Theories—An Introduction* (World Scientific, Singapore, 1992), p. 39.
[31] R. M. Woloshyn, T. Draper, K. F. Liu, and W. Wilcox, Phys. Rev. D **39**, 978 (1989).
[32] K. F. Liu, S. J. Dong, T. Draper, and W. Wilcox, Phys. Rev. Lett. **74**, 2172 (1995).